

AUXILIARY-CAVITY-INDUCED ULTRASENSITIVE AND ULTRAHIGH-RESOLUTION BIOMOLECULE MASS SENSING IN A HYBRID SPINNING RESONATOR SYSTEM

Hua-Jun Chen

School of Mechanics and Photoelectric Physics

Anhui University of Science and Technology

Huainan Anhui 232001, China

E-mail: aust_phy@163.com

Abstract

We theoretically demonstrate an ultrasensitive and ultrahigh-resolution biomolecule mass sensing based on a spinning resonator system, which includes a spinning whispering-gallery-mode (WGM) optomechanical cavity and an auxiliary optical cavity. When the WGM cavity is spinning along the clockwise or counterclockwise direction, the cavity field will undergo different Sagnac effect. If the Sagnac effect and the auxiliary optical cavity are simultaneously taken into consideration, not only the line width of the transmission spectrum is significantly squeezed, but also the transmission intensity will be extremely enhanced, which indicates an ultrasensitive and ultrahigh-resolution mass sensor. When the mass of external biomolecules (such as baculovirus or coronavirus) is deposited on the resonator, their mass can be determined by tracking the resonance frequency shifts in the transmission spectrum. Thus, our research can provide a method to classify kinds of viruses, especially can be used to identify 2019-nCoV.

Keywords: spinning resonator, mass sensing, auxiliary optical cavity.

1. Introduction

Optomechanical (OM) systems [1, 2], due to their significance in fundamental studies and potential applications, such as the ground state cooling [3–5], high-precision measurements [6–10], and quantum information processing [11–14], have drawn lots of attention in the past decades. Meanwhile, lots of significant phenomena, including phonon lasers [15–18], squeezing [19], nonreciprocity [20, 21], exceptional point [22, 23], optomechanically-induced transparency (OMIT) [24–27], and OMIT-induced slow-light effect [27, 28] have also been demonstrated in different OM systems. In numerous OM systems, whispering-gallery-mode (WGM) optical cavities are representative-cavity OM systems, due to their high-quality factors and small mode volumes enabling strong light–matter interactions. Then, WGM OM systems are used to investigated OMIT [25], cooling the resonator to the ground state [3, 29], mass sensing [30], and so on. In WGM-cavity OM systems, the light in WGM cavity will exert a radial force on the cavity sidewalls, which induces the mechanical mode expanding and shrinking continuously termed as radial breathing mode [6]. Therefore, the optomechanical interactions generate, which result in remarkable quantum interference effects. A recent advance closely related to our present work here is mass sensing [30–34] based on WGM optical microresonators.

Recently, a spinning WGM OM system was proposed [35], and OMIT was theoretically demonstrated in the system. Soon after, the spinning WGM resonator has been experimentally demonstrated [36], and then lots of phenomena and applications, such as the phonon laser [37,38], nonreciprocity [39,40], photon blockades [41–43], entanglement [44], and nanoparticle sensing [45], have been investigated in the spinning WGM resonator system. Although mass sensing was proposed before in the spinning WGM resonator system [45], the optomechanical effect was not considered. Here, considering the optomechanical effect, we present an ultrasensitive and ultrahigh-resolution biomolecule mass sensing based on the spinning WGM OM system with an auxiliary optical cavity, which has not yet been explored, to the best of our knowledge.

For the mass sensing, a typical means is the observation of the resonance frequency shift of the optical cavity, when nanoparticles are attached to the optical resonator [46]; additionally, the ultrasensitive size sensing has been demonstrated with inspecting the shift of optical cavities [47,48]. Afterwards, several different sensing regimes, such as the line-width change [49], mode splitting [50,51], and mode broadening [52], were also demonstrated. On the other hand, the other alternative scheme for mass sensing depends on reading out directly the small mass of the nanoparticles [53–56], with the relationship $\delta m \approx \frac{\partial M}{\partial \omega_m} = R^{-1} \delta f$, where R^{-1} is the mass responsivity [56] with the added mass δm , the frequency ω_m , and the effective mass M of the resonator. Similar to the mass sensing demonstrated in [34,53–55], in this paper, we introduce an auxiliary optical cavity in the spinning WGM OM system and present an ultrasensitive and ultrahigh-resolution biomolecule-mass sensing scheme based on monitoring the frequency shift of the mechanical resonator, which is similar to the mass sensing demonstrated in [34,53–55]. The transmission is tunable with controlling the WGM cavity rotating along the clockwise (CW) and counterclockwise (CCW) directions due to the Sagnac shift, and the results indicate that the CW direction rotation enhances the intensity of the transmission, while the CCW direction rotation restrains the transmission. When an auxiliary optical cavity is taken into consideration, combining with the cavity–cavity coupling and the CW direction rotation of the WGM cavity, we find that not only the intensity of the transmission is enhanced acutely but also the full width at a half maximum (FWHM) is significantly squeezed, which indicates a high resolution and ultrasensitive mass sensor based on the hybrid spinning OM system.

2. Model and Theory

The model to be considered is shown in Fig. 1, which includes an optomechanical cavity **a** and an auxiliary optical cavity **c**. The OM cavity **a**, with resonance frequency ω_a and intrinsic loss rate κ_a , is evanescently coupled to a tapered fiber, and the laser field in the cavity **a** induces a mechanical breathing mode due to the radiation pressure, which is described by a mechanical mode with the mechanical frequency ω_m . Then, the optomechanical interaction is described by the Hamiltonian $H_{\text{om}} = -\hbar g a^\dagger a x$, where $a^\dagger(a)$ and $b^\dagger(b)$ are the creation (annihilation) operators of the cavity mode **a** and the mechanical mode, respectively, and g gives the coupling strength between the cavity field **a** and the mechanical resonator. The cavity **c** is an auxiliary optical cavity, with resonance frequency ω_c and intrinsic loss rate κ_c . The coupling between cavity **a** and cavity **c** is similar to the Jaynes–Cummings Hamiltonian $H_{\mathbf{a}-\mathbf{c}} = \hbar J (a^\dagger c + a c^\dagger)$. The WGM OM cavity **a** is rotating with an angular velocity Ω , then the light circulating in the resonator experiences a Sagnac–Fizeau shift [35,36], i.e., $\omega_a \rightarrow \omega_a + \Delta_{\text{sag}}$, where

$\Delta_{\text{sag}} = \pm \frac{nR\Omega\omega_a}{c} \left(1 - \frac{1}{n^2} - \frac{\lambda}{n} \frac{dn}{d\lambda} \right) \equiv \pm \eta\Omega$, with the refractive index n , the radius of the WGM cavity R , the speed c , and the wavelength λ of light in vacuum.

Generally, the dispersion term $\frac{dn}{d\lambda}$, originated from the relativistic correction of the Sagnac effect, is quite small. Assuming that the WGM OM system can rotate along the CW and CCW directions, we use $\Delta_{\text{sag}} > 0$ and $\Delta_{\text{sag}} < 0$ to describe the WGM cavity rotating along the CW and CCW directions, respectively; see Fig. 1.

We use a strong pump field with frequency ω_p and a weak probe field with frequency ω_s to drive the OM cavity a ; the amplitudes of the pump field (probe field) are $\varepsilon_p = \sqrt{P_a/\hbar\omega_p}$ ($\varepsilon_s = \sqrt{P_s/\hbar\omega_s}$), where P_a (P_s) is the pump (probe) field power. The auxiliary optical cavity c is driven by a driven field with frequency ω_p , and the driven amplitude is $\varepsilon_d = \sqrt{P_d/\hbar\omega_p}$. Then, the interaction Hamiltonian between the two WGM cavities and the laser fields reads

$$H_{\text{dri}} = i\hbar\sqrt{\kappa_{ae}}\varepsilon_p \left(a^\dagger e^{-i\omega_p t} - a e^{i\omega_p t} \right) + i\hbar\sqrt{\kappa_{ae}}\varepsilon_s \left(a^\dagger e^{-i\omega_s t} - a e^{i\omega_s t} \right) + i\hbar\sqrt{\kappa_{ce}}\varepsilon_d \left(a^\dagger e^{-i\omega_p t} - a e^{i\omega_p t} \right),$$

where κ_{ae} and κ_{ce} describe the extra loss rate.

In a frame rotating at the pump field frequency ω_p , we obtain the Hamiltonian of the hybrid system as follows:

$$H = \hbar\Delta a^\dagger a + \hbar\Delta_c c^\dagger c + \left(\frac{p^2}{2M} + \frac{1}{2}\omega_m^2 x^2 \right) + \frac{p_\theta^2}{2MR^2} + H_{\text{om}} + H_{\mathbf{a}-\mathbf{c}} + H_{\text{dri}}, \quad (1)$$

where $a^\dagger(a)$ is the creation (annihilation) operator of the OM cavity \mathbf{a} , and $c^\dagger(c)$ is the creation (annihilation) operator for cavity \mathbf{c} ; also, $\Delta = \omega_a - \omega_p + \Delta_{\text{sag}} = \Delta_a + \Delta_{\text{sag}}$ is the detuning between the OM cavity \mathbf{a} and the pump field, $\Delta_c = \omega_c - \omega_p$ is the detuning between cavity \mathbf{c} and the driven field, $x(p)$ is the displacement (momentum) operator of the mechanical resonator with the commutation relation $[x, p] = i$, $g = \omega_a/R$ is the optomechanical coupling, while θ and p_θ mean the rotation angle and angular momentum operator with the commutation relation $[\theta, p_\theta] = i$ [35]. Then, the Langevin equations of the hybrid spinning OM system read

$$\dot{a} = -(i\Delta + \kappa_a)a + igax - iJc + \sqrt{\kappa_{ae}}(\varepsilon_p + \varepsilon_s e^{-i\delta t})m, \quad (2)$$

$$\dot{c} = -(i\Delta_c + \kappa_c)c - iJa + \sqrt{\kappa_{ce}}\varepsilon_d, \quad (3)$$

$$\ddot{x} + \gamma_m \dot{x} + \omega_m^2 x = \frac{\hbar g}{M} a^\dagger a + \frac{p_\theta^2}{M^2 R^3}, \quad (4)$$

$$\dot{\theta} = \frac{p_\theta}{MR^2}, \quad \dot{p}_\theta = 0, \quad (5)$$

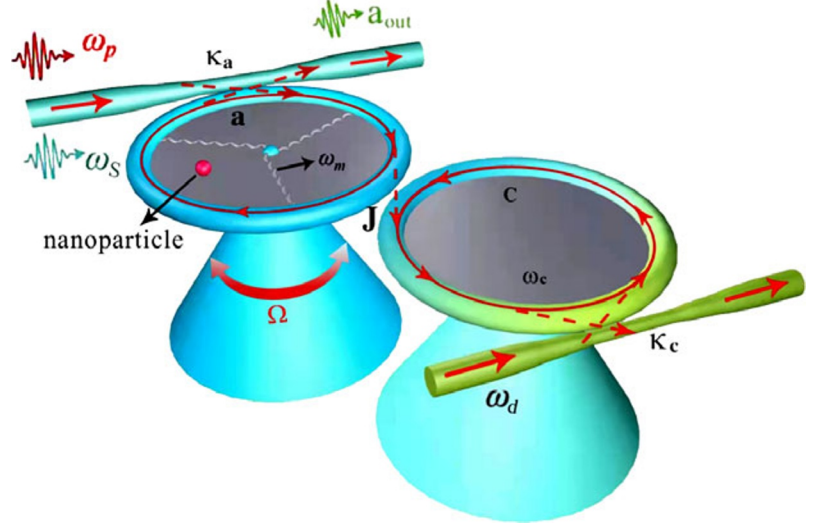


Fig. 1. Schematic diagram of the hybrid spinning WGM OM system, which includes an OM cavity spinning along the CW and CCW directions \mathbf{a} , and an auxiliary optical cavity \mathbf{c} . Nanoparticles are landed on the OM cavity \mathbf{a} .

where γ_m is the mechanical resonator damping rate. Since the pump field is stronger than the probe field, the dynamics can be linearized by expanding each operator as a sum of its steady-state value and a small fluctuation around it, with the transform $\rho = \rho_s + \delta\rho$ that indicates the operators a , c , and x . After substituting the division forms into Eqs. (2)–(5), we obtain the steady state solutions of the variables of $(i\Delta' + \kappa_a)a_s + iJc_s = \sqrt{\kappa_{ae}}\varepsilon_p$, $(i\Delta_c + \kappa_c)c_s + iJa_s = \sqrt{\kappa_{ce}}\varepsilon_d$, and $x_s = (\hbar g|a_s|^2/M\omega_m^2) + (R\Omega^2/\omega_m^2)$, where $\Omega = \frac{d\theta}{dt}$ is the angular velocity of the spinning resonator, and $\Delta' = \Delta - g x_s$ is the effective detuning. It is obvious that the three equations together determine the mechanical displacement x_s , the intracavity photon number $|a_s|^2$, and $|c_s|^2$.

Assuming that the pump field is sufficiently strong, all the operators can be identified with their expectation values, in view of the mean-field approximation, $\langle Qc \rangle = \langle Q \rangle \langle c \rangle$ [24]. Then, we obtain the linearized Langevin equations for the expectation values with neglecting nonlinear terms in the fluctuations; they read

$$\langle \delta \dot{a} \rangle = -(i\Delta' + \kappa_a)\langle \delta a \rangle + i g a_s \langle \delta x \rangle - i J \langle \delta c \rangle + \sqrt{\kappa_{ae}} \varepsilon_s e^{-i\delta t}, \quad (6)$$

$$\langle \delta \dot{c} \rangle = -(i\Delta_c + \kappa_c)\langle \delta c \rangle - i J \langle \delta a \rangle, \quad (7)$$

$$\langle \delta \ddot{x} \rangle + \gamma_m \langle \delta \dot{x} \rangle + \omega_m^2 \langle \delta x \rangle = \frac{\hbar g}{M} (a_s^* \langle \delta a \rangle + a_s \langle \delta a^+ \rangle). \quad (8)$$

In order to solve Eqs. (6)–(8), we make the ansatz as $\langle \delta \rho \rangle = \rho_+ e^{-i\delta t} + \rho_- e^{i\delta t}$ and, substituting them into above equations with ignoring the high-order terms and working to the lowest order in ε_s but to all orders in ε_p , we arrive at

$$a_+ = \frac{(\kappa_a - i\Lambda_2)\sqrt{\kappa_{ae}}\varepsilon_s}{(\kappa_a + i\Lambda_1)(\kappa_a - i\Lambda_2) - \hbar^2 g^4 |a_s|^4 \chi^2}, \quad (9)$$

where $\theta_1 = -iJ/[\kappa_c + i(\Delta_c - \delta)]$, $\theta_2 = -iJ/[\kappa_c - i(\Delta_c + \delta)]$, and $\chi = 1/M(\omega_m^2 - i\delta\gamma_m - \delta^2)$, with $\Lambda_1 = \Delta' - \delta + J\theta_1 - \hbar g^2 \chi |a_s|^2$ and $\Lambda_2 = \Delta' + \delta + J\theta_2 - \hbar g^2 \chi |a_s|^2$. In view of the standard input–output relation $a_{\text{out}}(t) = a_{\text{in}} - \sqrt{2\kappa_a}a(t)$, where $a_{\text{out}}(t)$ is the output field operator, the transmission rate of the probe field is [24–27]

$$T(\omega_s) = |t(\omega_s)|^2 = \left| \frac{a_{\text{out}}(t)}{a_{\text{in}}(t)} \right|^2 = \left| 1 - \frac{\sqrt{\kappa_{ae}}}{\varepsilon_s} a_+ \right|. \quad (10)$$

3. Numerical Results and Discussion

In our numerical calculations, we use the experimentally feasible values [35, 57], namely, $M = 20$ ng, $\omega_m = 200$ MHz, $\gamma_m = 0.2$ MHz, $\lambda = 1.55$ μm , $n = 1.44$, $c = 3 \cdot 10^8$ m/s, $\omega_c = 193.5$ THz, $Q = \frac{\omega_a}{\kappa_a} = 3 \cdot 10^7$, $R = 0.25$ mm, $P_a = 0.01$ W, $P_d = 0.01$ W, $\Omega = 10$ kHz, and $J = 0.5 \kappa_a$.

In Fig. 2, we give the probe transmission spectra under different parameter regimes, i.e., ($J = 0$ or $J \neq 0$) and ($\Omega < 0$ or $\Omega > 0$), with unchanged optomechanical coupling g and the pump power P_a and P_d in the condition of $\Delta_a = 0$ and $\Delta_c = -\omega_m$. In Fig. 2a, we first give the probe transmission spectrum as a function of the probe–cavity detuning $\Delta_s = \omega_s - \omega_a$, in the case of $J = 0$ and $\Omega = 0$, i.e., the OM cavity is stationary, and we do not consider the auxiliary optical cavity. There are two sharp sideband peaks exactly locating at $\Delta_s = \pm\omega_m$ ($\omega_m = 200$ MHz) in the transmission spectrum, and there is also a broad transmission dip around $\Delta_s = 0$ corresponding to the cavity absorption, which gives a method to determine the resonator frequency. These results have been demonstrated and the physical mechanism

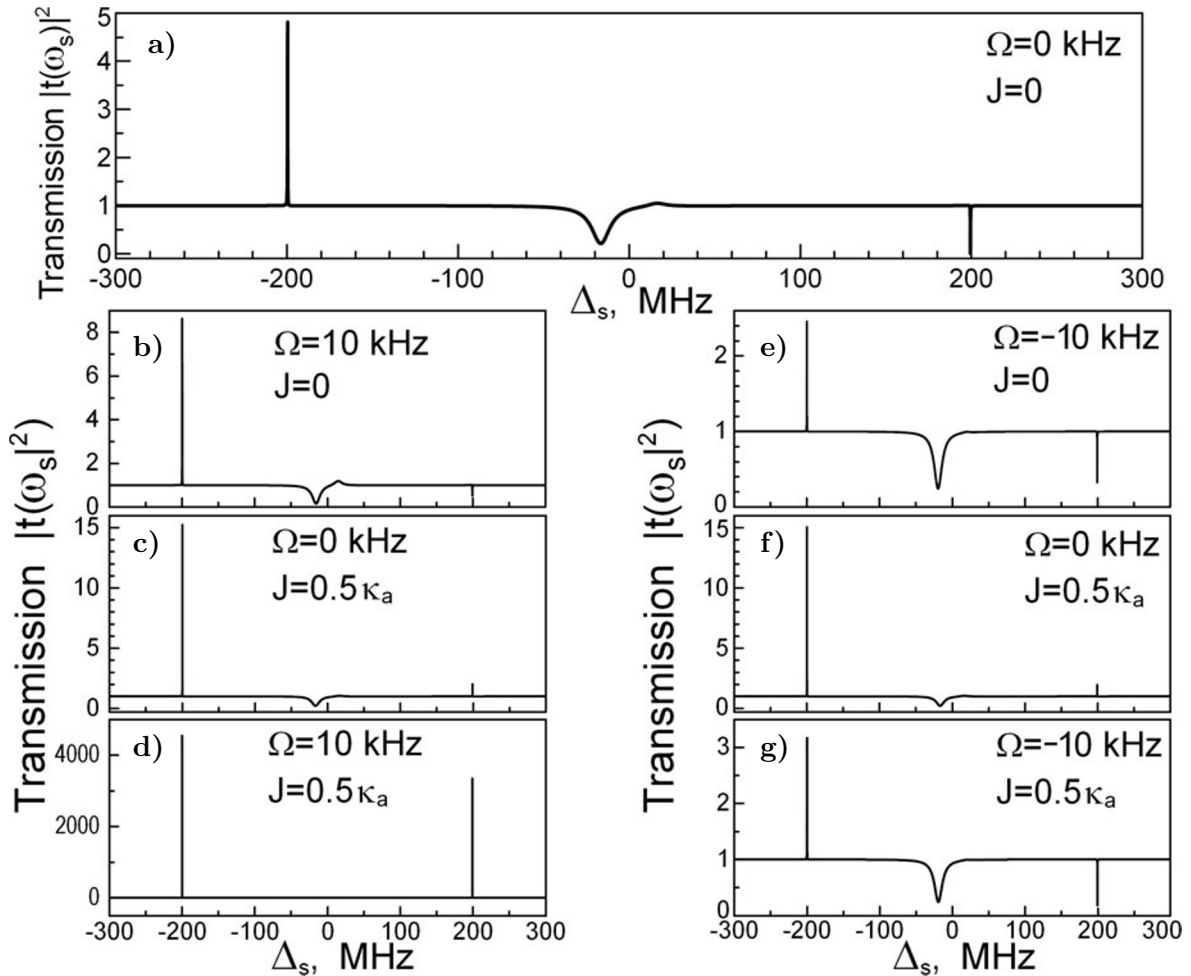


Fig. 2. The transmission spectrum as a function of the probe-cavity detuning $\Delta_s = \omega_s - \omega_a$ under different parameters condition; here, $\Omega = 0$ and $J = 0$ (a), $\Omega = 10$ kHz and $J = 0$ (b), $\Omega = 0$ and $J = 0.5\kappa_a$ (c), $\Omega = 10$ kHz and $J = 0.5\kappa_a$ (d), $\Omega = -10$ kHz and $J = 0$ (e), $\Omega = 0$ and $J = 0.5\kappa_a$ (f), and $\Omega = -10$ kHz and $J = 0.5\kappa_a$ (g).

also been elaborated in [34]. Here, we are much more interested in the case where the WGM cavity is spinning; also an auxiliary optical cavity is taken into consideration. In Fig. 2 b, d, we set the WGM cavity spinning along CW and CCW directions, respectively, and do not consider the auxiliary optical cavity, i.e., the parameters are $\Omega \neq 0$ and $J = 0$. Compared with Fig. 2 a, we can find that, if WGM OM cavity is spinning along the CW direction, the intensity of the transmission spectrum is enhanced; if WGM OM cavity is spinning along the CCW direction, the intensity of the transmission spectrum is receded. In Fig. 2 c, e, we set the WGM cavity to be stationary, while consider an auxiliary optical cavity, i.e., $\Omega = 0$ and $J = 0.5\kappa_a$; it is obvious that the intensity of the transmission is observably enhanced compared with Fig. 2 a. Since both the rotation of the WGM cavity and the auxiliary optical cavity can influence the intensity of the transmission spectrum, then in Fig. 2 d, f, we set the WGM cavity spinning along CW and CCW direction, respectively; meanwhile, we also introduce an auxiliary optical cavity, i.e., the parameters are $\Omega \neq 0$ and $J \neq 0$. It is obvious that, when the WGM cavity is spinning along the CW direction, the intensity of the transmission spectrum is tremendously enhanced, while if the WGM cavity

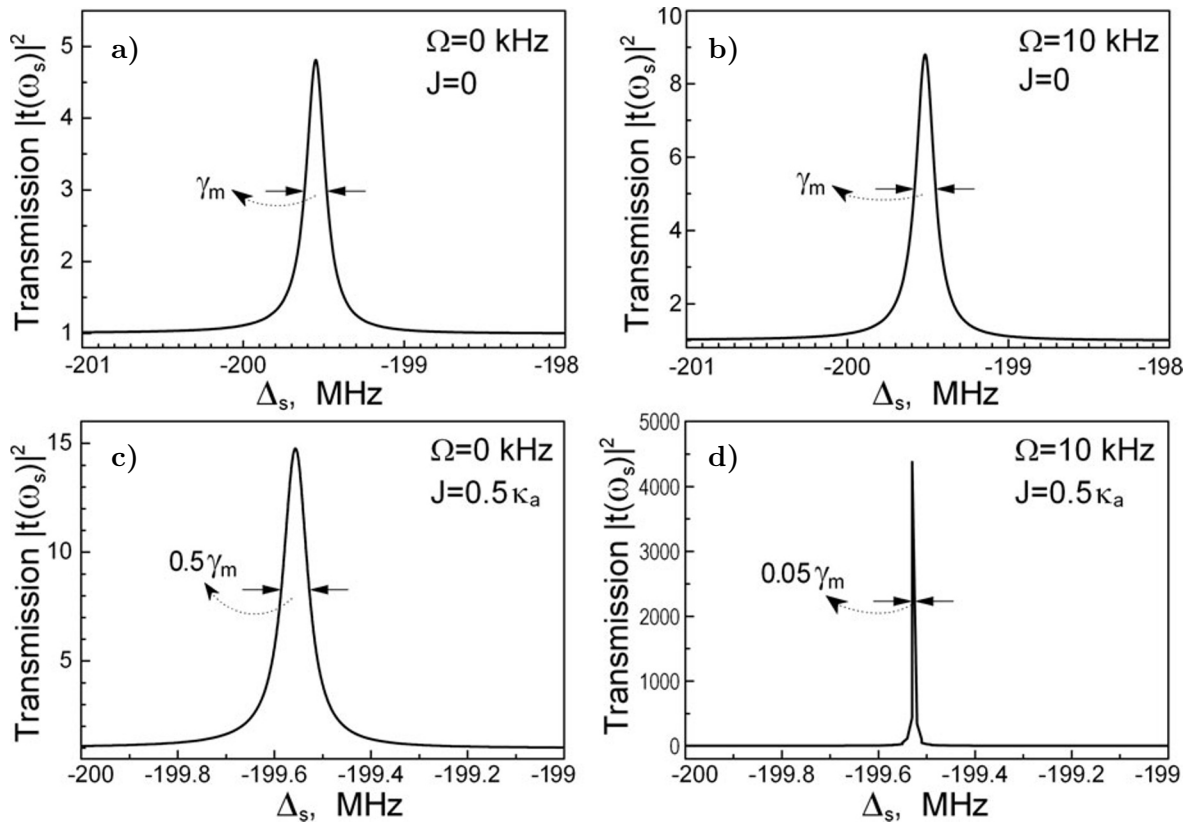


Fig. 3. The amplification of the transmission spectrum in Fig. 2 around $\Delta_s \simeq -\omega_m$ under different parameter condition; here, $\Omega = 0$ and $J = 0$ (a), $\Omega = 10$ kHz and $J = 0$ (b), $\Omega = 0$ and $J = 0.5\kappa_a$ (c), and $\Omega = 10$ kHz and $J = 0.5\kappa_a$ (d).

is spinning along the CCW direction rotation, the intensity of the transmission spectrum is weakened.

In order to obtain the ultrasensitive and high-resolution mass sensing, the spectral line width should be narrow for the line width of the transmission spectrum that determines the sensitivity of the mass sensing. In Fig. 3, we amplify the left peaks of the transmission spectra located at $\Delta_s \simeq -\omega_m$ in Fig. 2, and then measure their line widths under different parameters. According to Fig. 2, we find that the intensity of the sideband peaks in the transmission spectra in the condition of $\Omega > 0$ is enhanced much more significant than in the case of $\Omega < 0$; thus, in Fig. 3, we only investigate the transmission spectra in the condition of $\Omega > 0$. Not only the spinning direction of the WGM cavity but also the auxiliary optical cavity together affect the transmission spectra, and we investigate the two parameters that influence the transmission spectra under different parameter regimes. In Fig. 3 a, the parameter conditions are $\Omega = 0$ and $J = 0$, and the line width of the transmission spectrum is the damping rate γ_m of the mechanical resonator, which has been demonstrated in OM systems [34, 53–55]. If the WGM cavity is spinning, for example, $\Omega = 10$ kHz as shown in Fig. 3 b, with the parameter of $J = 0$, we can obtain that, although the line width does not change, the intensity of the sideband peak is observably enhanced. In Fig. 3 c, when the parameters are $\Omega = 0$ and $J = 0.5\kappa_a$, not only the line width is squeezed ($0.5\gamma_m$) but also the intensity of the sideband peak is enhanced compared with Fig. 3 a, b. Then, in Fig. 3 d, the parameters are $\Omega = 10$ kHz and $J = 0.5\kappa_a$, and it is obvious that the line width is further squeezed to $0.05\gamma_m$,

with an extremely enhanced intensity of the sideband peak in the transmission spectrum. Therefore, the spinning direction of the WGM cavity and the auxiliary optical cavity together permit ultrasensitive and ultrahigh-resolution mass sensor based on the hybrid spinning resonator system.

Then, we use the hybrid spinning resonator system to measure the mass of biomolecules (such as baculovirus or coronavirus), with the parameters $\Omega = 10$ kHz and $J = 0.5 \kappa_a$. Similar to the mass sensing demonstrated in [34, 53–55], the mass sensing based on the hybrid spinning OM system also depends on monitoring the frequency shift of the mechanical resonator, when nanoparticles are deposited on the resonator. The frequency shift depends on both the nanoparticles mass and landed position; here, we consider that nanoparticles are uniformly distributed on the WGM resonator and do not affect the spring constant of the resonator. The linear relationship of the external mass of nanoparticles and frequency shift of mechanical resonator is $\delta m \approx \frac{\partial M}{\partial \omega_m} = -\frac{\omega_m}{2M} \delta f$. If we put the nanoparticles on the WGM resonator; see Fig. 1, the total effective mass of the OM resonator would be increased, which results in the reduction of the resonance frequency and, as a result, in the frequency-shift generation.

Figure 4 gives the measure of nanoparticles, such as baculovirus, coronavirus, and 2019-nCoV; here, the black curve gives the transmission spectrum at $\Delta_s \simeq -\omega_m$ without considering any nanoparticles deposited on the WGM resonator, i.e., the bare resonator. If nanoparticles are deposited on the spinning WGM resonator, due to the increased mass of the nanoparticles, the transmission spectra show a frequency shift; see color curves, where 0.4 pg (1 pg = 10^{-12} g) nanoparticles can be observed in the hybrid spinning WGM resonator, which is much more sensitive than previous schemes [34, 53–55]. In addition, the bigger nanoparticles will lead to more distinct frequency shifts; in the inset, we also present the relationship of the frequency shifts and nanoparticles mass deposited on the spinning WGM resonator. The negative slope indicates the mass sensitivity of the resonator and, in the spinning WGM resonator, the mass responsivity is $|R| = 10^{16}$ Hz/g.

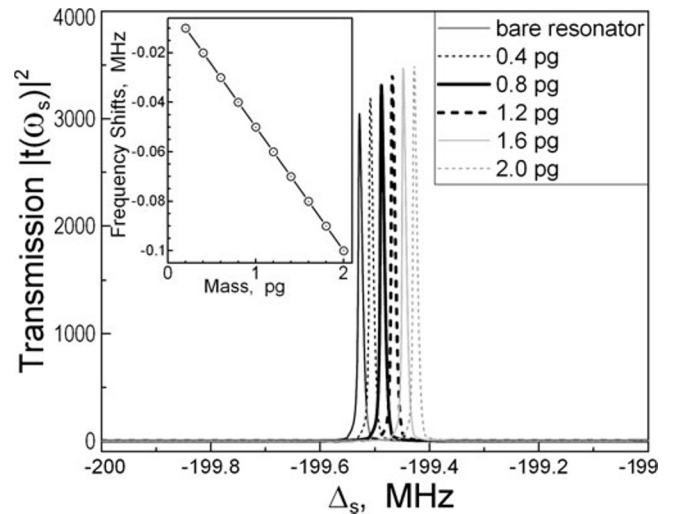


Fig. 4. The transmission spectra before and after depositing nanoparticles on the WGM resonator; here, the frequency-shifts are given by different curves. The inset shows the linear relationship between the frequency shifts and the mass of nanoparticles.

4. Summary

We theoretically proposed a high-resolution biomolecule mass sensor based on a hybrid spinning WGM resonator, where the OM WGM cavity was driven by a strong pump field and a weak probe field, and the auxiliary optical cavity was driven by a driven field. Due to the rotation of the WGM resonator along the CW and CCW directions, the Sagnac frequency shift influenced the probe transmission spectrum. Combining the Sagnac shift and the auxiliary optical cavity, we showed an ultrasensitive and ultrahigh-resolution mass sensing scheme to measure the external biomolecule mass (such as baculovirus or coronavirus) deposited on the WGM resonator, which depended on tracking the resonance frequency

shifts in the probe transmission spectrum. The proposal presented here not only provides a method to classify different viruses but also be used to identify 2019-nCoV.

Acknowledgments

The author acknowledges the financial support of the National Natural Science Foundation of China under Grants Nos. 11647001 and 11804004, the China Postdoctoral Science Foundation under Project No. 2020M681973, and the Anhui Provincial Natural Science Foundation under Grant No. 1708085QA11.

References

1. M. Aspelmeyer, T. J. Kippenberg, and F. Marquardt, *Rev. Mod. Phys.*, **86**, 1391 (2014).
2. M. Metcalfe, *App. Phys. Rev.*, **1**, 031105 (2014).
3. A. Schliesser, R. Riviere, G. Anetsberger, et al., *Nat. Phys.*, **4**, 415 (2008).
4. J. D. Teufel, T. Donner, D. Li, et al., *Nature (London)*, **475**, 359 (2011).
5. J. Chan, T. P. M. Alegre, A. H. Safavi-Naeini, et al., *Nature (London)*, **478**, 89 (2011).
6. A. Schliesser, O. Arcizet, R. Riviere, et al., *Nat. Phys.*, **5**, 509 (2009).
7. E. Gavartin, P. Verlot, and T. J. Kippenberg, *Nat. Nanotechnol.*, **7**, 509 (2012).
8. A. G. Krause, M. Winger, T. D. Blasius, et al., *Nat. Photonics*, **6**, 768 (2012).
9. S. Schreppler, N. Spethmann, N. Brahms, et al., *Science*, **344**, 1486 (2014).
10. N. Matsumoto, S. B. Catano-Lopez, M. Sugawara, et al., *Phys. Rev. Lett.*, **122**, 071101 (2019).
11. Y. D. Wang and A. A. Clerk, *Phys. Rev. Lett.*, **108**, 153603 (2012).
12. L. Tian, *Phys. Rev. Lett.*, **108**, 153604 (2012).
13. L. Tian, *Phys. Rev. Lett.*, **110**, 233602 (2013).
14. Y. D. Wang and A. A. Clerk, *Phys. Rev. Lett.*, **110**, 253601 (2013).
15. I. S. Grudinin, H. Lee, O. Painter et al., *Phys. Rev. Lett.*, **104**, 083901 (2010).
16. H. Jing, S. K. Ozdemir, X. Y. Lu, et al., *Phys. Rev. Lett.*, **113**, 053604 (2014).
17. H. Lu, S. K. Ozdemir, L. M. Kuang, et al., *Phys. Rev. Appl.*, **8**, 044020 (2017).
18. J. Zhang, B. Peng, S. K. Ozdemir, et al., *Nat. Photonics*, **12**, 479 (2018).
19. A. H. Safavi-Naeini, S. Groeblacher, J. T. Hill, et al., *Nature (London)*, **500**, 185 (2013).
20. S. Manipatruni, J. T. Robinson, and M. Lipson, *Phys. Rev. Lett.*, **102**, 213903 (2009).
21. X. W. Xu, Y. Li, A. X. Chen, et al., *Phys. Rev. A*, **93**, 023827 (2016).
22. X.-Y. Lu, H. Jing, J.-Y. Ma, et al., *Phys. Rev. Lett.*, **114**, 253601 (2015).
23. H. Xu, D. Mason, L. Jiang, et al., *Nature (London)*, **537**, 80 (2016).
24. G. S. Agarwal and S. Huang, *Phys. Rev. A*, **81**, 041803 (2010).
25. S. Weis, R. Riviere, S. Deleglise, et al., *Science*, **330**, 1520 (2010).
26. J. D. Teufel, D. Li, M. S. Allman, et al., *Nature (London)*, **471**, 204 (2011).
27. A. H. Safavi-Naeini, T. P. M. Alegre, J. Chan, et al., *Nature (London)*, **472**, 69(2011).
28. X. Zhou, F. Hocke, A. Schliesser, et al., *Nat. Phys.*, **9**, 179 (2013).
29. R. Riviere, S. Deleglise, S. Weis, et al., *Phys. Rev. A*, **83**, 063835 (2011).
30. F. Liu, S. Alaie, Z. C. Leseman, et al., *Opt. Exp.*, **21**, 19555 (2013).
31. J. Zhu, S. K. Ozdemir, Y. F. Xiao, et al., *Nat. Photonics*, **4**, 46 (2010).
32. H. Jing, H. Lu, S. K. Ozdemir, et al., *Optica*, **5**, 1424 (2018).
33. X. Jiang, A. J. Qavi, S. H. Huang, et al., *Matter*, **3**, 371 (2020).
34. H. J. Chen, *Appl. Phys. Express*, **14**, 082005 (2021).
35. H. Lu, Y. Jiang, Y. Z. Wang, et al., *Photonics Res.*, **5**, 367 (2017).
36. S. Maayani, R. Dahan, Y. Kligerman, et al., *Nature (London)*, **558**, 569 (2018).
37. Y. Jiang, S. Maayani, T. Carmon, et al., *Phys. Rev. Appl.*, **10**, 064037 (2018).

38. Y. Xu, J. Y. Liu, W. Liu, et al., *Phys. Rev. A*, **103**, 053501 (2021).
39. W.-A. Li, G.-Y. Huang, J.-P. Chen, et al., *Phys. Rev. A*, **102**, 033526 (2020).
40. X. Xu, Y. Zhao, H. Wang, et al., *Photonics Res.*, **8**, 143 (2020).
41. R. Huang, A. Miranowicz, J.-Q. Liao, et al., *Phys. Rev. Lett.*, **121**, 153601 (2018).
42. B.-J. Li, R. Huang, X.-W. Xu, et al., *Photon. Res.*, **7**, 630 (2019).
43. K. Wang, Q. Wu, Y. F. Yu, et al., *Phys. Rev. A*, **100**, 053832 (2019).
44. Y.-F. Jiao, S.-D. Zhang, Y.-L. Zhang, et al., *Phys. Rev. Lett.*, **125**, 143605 (2020).
45. H. Jing, H. Lu, S. K. Ozdemir, et al., *Optica*, **5**, 1424 (2018).
46. Y. Zhi, X. C. Yu, Q. Gong, et al., *Adv. Mater.*, **29**, 1604920 (2017).
47. A. M. Armani, R. P. Kulkarni, S. E. Fraser, et al., *Science*, **317**, 783 (2007).
48. F. Vollmer and S. Arnold, *Nat. Meth.*, **5**, 591 (2008)
49. B. Q. Shen, X. C. Yu, Y. Zhi, et al., *Phys. Rev. Appl.*, **5**, 024011 (2016).
50. F. Vollmer and L. Yang, *Nanophotonics*, **1**, 267 (2012).
51. L. He, S. K. Ozdemir, J. Zhu, et al., *Nat. Nanotechnol.*, **6**, 428 (2011).
52. L. Shao, X. F. Jiang, X. C. Yu, et al., *Adv. Mater.*, **25**, 5616 (2013).
53. J. J. Li and K. D. Zhu, *Phys. Rep.*, **525**, 223 (2013).
54. C. Jiang, Y. Cui, and K. D. Zhu, *Opt. Express*, **22**, 13773 (2014).
55. Y. He, *Appl. Phys. Lett.*, **106**, 121905 (2015).
56. K. L. Ekinici, Y. T. Yang, and M. L. Roukes, *J. Appl. Phys.*, **95**, 2682 (2004).
57. H. Guo, M. Karpov, and E. Lucas, *Nat. Phys.*, **13**, 94 (2017).